International Journal of Soft Computing 2 (4): 502-512, 2007

Tissue Characterization of Kidney using Content Descriptive Power Spectral Components for Computer-Aided Diagnosis and Classification

[1]K. Bommanna Raja, [2]M. Madheswaran and [1]K. Thyagarajah
[1]Department of Electronics and Communication Engineering, Centre for Research and Development, PSNA College of Engineering and Technology, Dindigul-624 622, TamilNadu, India
[2]Department of Electronics and Communication Engineering, Centre for Advanced Research, Muthyammal Engineering College, Rasipuram-637 187, TamilNadu, India

Abstract: The objective of this study is to classify few important kidney categories by characterizing the tissues of kidney region using the unique power spectral features with ultrasound as imaging modality. The images are acquired from male and female subjects of age 45±15 years. Three kidney categories namely normal, medical renal diseases and cortical cyst are considered for the analysis. The acquired images are initially pre-processed to retain the pixels-of-interest. The proposed features depend on the spatial distribution of spectral components in the kidney region. A set of power spectral features $P_T^{W_1}$, $P_T^{W_2}$, $P_{T-W_{12}}^{R_1}$, $P_{T-W_{12}}^{R_2}$, $p_{T-W_{1d}}^{R_3}$ and $P_{T-W_{1d}}^{R_4}$ are estimated at the specific cut-off frequencies Ω_{rc1} and Ω_{rc2} in the spectrum and by considering global mean total power. The results obtained show that the features are highly content descriptive and provide discrete range of values for each kidney category. Such isolated feature values facilitate to identify the kidney categories objectively which may be used as a secondary observer. The proposed method and features also explores the possibility of implementing computer-aided diagnosis system exclusively for US kidney images.

Key words: US kidney image analysis, image processing, image segmentation, feature extraction-power spectrum analysis, kidney classification, computer, aided diagnosis

INTRODUCTION

The known facts of abdominal Ultrasound (US) imaging like real-time, non-invasive, non-radioactive and inexpensive properties makes it to find wide spread application in diagnosing soft tissue organ such as kidney (Hangen, 1995; Pollack and Mcclennan, 2000). The extensive use of computational knowledge to analyze the US kidney images the researchers in this area have long sought to extract features for the characterization of kidney tissue. In general diagnostic studies of US images are subjective and the resultant performance suffers from intra and inter-observer variability. Because unlike all imaging modalities, US imaging is subject to number of artifacts that degrade image quality and compromise diagnostic confidence (Huang *et al*., 2004). The major performance limiting factor in visual perception of US imaging is a multiplicative noise called speckle that makes the signal or lesion difficult to detect (Loi zou *et al*., 2002; Eslami *et al*., 2005). Also other factors that compounds are viewing distance, display size, resolution, brightness, contrast, sharpness, colorfulness and naturalness (Loizou *et al*., 2005). Due to these constraints the possibility of segmentation of kidney region and hence the extraction of features that helps to evaluate the tissue characteristic of kidney objectively becomes difficult.

The term Computer-Aided Diagnosis (CAD) refers to the use of computers to assist doctors in objective decision making. Although the kidney related diseases are extremely common in adults they are not adequately reported in CAD hitherto (Loizou *et al*., 2002; Eslami *et al*., 2005). If a method that provides content descriptive features exist then a CAD system to meet the following requirements: Establishing a quantitative universal reference for the US kidney images. implementing Image Retrieval in Medical Application (IRMA) system, making comparative study on images for objective decision, developing an expert system that automatically recognizes the extent of pathology or

Corresponding Author: K. Bommanna Raja, Department of Electronics and Communication Engineering, Centre for Research and Development, PSNA College of Engineering and Technology, Dindigul-624 622, TamilNadu, India

normality and examining extent of healing or failure under post-therapy observation may be realized in practice (Bommanna *et al*., 2003; Karthikeyini *et al*., 2004). The extraction of content descriptive features may not be possible unless a general segmentation scheme for contouring the kidney region of different categories in US images is available. Hence the implementation of CAD system initially requires a general segmentation scheme which is then followed by the evaluation of content descriptive features. The solution to develop such system is in high demand and not been reported until now.

Most of the study on US kidney images so far deals with the segmentation of the kidney region using various methodologies (Eslami *et al*., 2005; Bakker *et al*., 1997; Matre *et al*., 1999; Jun *et al*., 2005; Marcos and Carlos, 2005; Abouzar *et al*., 2004). Though the performance of these methods is well appreciated, they fail to formulate a general scheme by considering various kidney categories. The local features used for finding optimum contour are to be further investigated to explore their potential in describing the global characteristic of kidney so that the CAD system is made realistic. The authors proposed a higher order spline interpolation obtained with up-sampling of homogeneously distributed co-ordinate (i-HSIC) segmentation scheme to contour the kidney region of different categories (Bommanna *et al*., 2007). This method helps, in specific, to retain the Pixels-of-Interest (POI) i.e., the pixels of kidney region and may be used as a general segmentation scheme.

The spectral features estimated by using Fast Fourier Transform (FFT) have been used for various analysis, diagnosis and evaluation of biological system. Veenland *et al.* (1998) performed Fourier power spectrum analysis to study the effect of image noise and blurring in tissue structures represented by textures in radiographs. Ciliary beat frequencies of respiratory epithelium cells were quantitatively measured and analyzed with maximum peak frequencies obtained by FFT power spectrum (Yi *et al*., 1997). Tokudome *et al.* (1999) assessed the role of autonomic nervous system in the regulation of basal coronary artery tone in normal and atherosclerotic plague segments by using intravascular ultrasound in human. They evaluated the sympathetic and vagal activities at rest as the integrated power of FFT spectrum for the low frequency and high frequency components, respectively. The characterization of atherosclerotic plague was made by using the parameters maximum power and spectral slope obtained from normalized power spectrum (Spencer *et al*., 1997). Using US as imaging method, Fukushima *et al.* (1997) established a computer-aided diagnosis system for diffuse liver diseases using annular Fourier power spectrum and longitudinal Fourier power spectrum as two of their seven parameters to train the artificial neural network. Differentiation of breast tumors as malignant and benign in vivo in patients with palpable breast masses and in vitro in excised breast tissue was made using ultrasound tissue characterization technique based on parameters evaluated from the power spectrum of back scattered echoes (Golub *et al*., 1993). Allemann *et al.* (1993) used US imaging and spectrum analysis to study the hyphema for distinguishing organized from fluid hyphema and recent from old hemorrhage in the eye. They concluded that spectrum analysis of high frequency ultrasound data was able to distinguish organized from recent hemorrhage which was clinically helpful for planning hyphema therapy. Spectrum analysis was also performed (Li *et al*., 2002) for detection of breast cancer using broadband microwave tomographic images. The in vitro study for assessing node status in lymph node (Feleppa *et al*., 1997) indicates that spectrum analysis offer excellent means of determining the presence of metastatic cancer. A new anistrophy index was measured (Barbara *et al*., 2005) using FFT to assess the bone structure with the help of trabecular bone radiographic images. Also trabecular bone structure was analyzed (Gregory *et al*., 1999) using Fourier transform to generate a spectral fingerprints of an image. Principle component analysis was then applied to identify the features from the Fourier transform and passed to a neural network for classification as osteoporosis and osteoarthritis. In a study on walking foot pressure images (Prabhu *et al*., 2001) for early detection of planar ulcers, the quantity power ratio is defined to distinguish between normal and diabetic feet at different levels of neuropathy. The review of study in the context of power spectrum analysis deliberates the potential of spectral components under varied environments and applications.

In this study an effort has been taken for the first time;

- To establish a new set of content descriptive features using power spectral components to classify different kidney category namely Normal (NR), Medical Renal Diseases (MRD) and Cortical Cyst (CC).
- To deal with the requirements and of the CAD system exclusively meant for US kidney images.

MATERIALS AND METHODS

Image data acquisition: The images used for the analysis are acquired from two types of scanning systems namely, ATL HDI 5000 curvilinear probe with transducer

frequency of 3-6 MHz and Wipro GE LOGIC 400 curvilinear probe with transducer frequency of 3-5 MHz. As the sonographic evaluation is made based on the distribution of echogenity that reflects tissue characteristics, for better echo visualization the longitudinal cross section of kidney is taken to include renal sinus, medulla and cortex regions as suggested by the experts. This also ensures better visual interpretation of the normal and diseased kidney. The transducer frequency is fixed at 4 MHz. In total, 150 images with 50 images in each category are obtained from male and female subjects of age 45±15 years. The images of both right and left kidneys are considered for the analysis. The kidney diseases are usually categorized as hereditary, congenital or acquired. The most common hereditary disorder is cystic diseases which includes simple renal cyst and complex renal cyst or poly cyst. The kidneys affected with these diseases are considered under CC category. The sonographic features of renal cyst include a well defined mass lesion, smooth wall and circular hypo echoic mass with good through transmission. Any congenital or acquired kidney diseases typically cause renal infection and/or destruction of kidney tissues that may lead to end stage chronic renal failure are considered under MRD category. Due to tissue destruction, anatomical separation between renal sinus, medulla and cortex becomes difficult. The sonographic evaluation shows hyper echoic kidney region with increased cortical echogenity and differentiation between cortex and collecting system is poor. The sample US kidney images of NR, MRD and CC are shown in the Fig. 1. It can be seen that ultrasound shows appreciable renal border in all three cases, but internally due to pathology involved the echogenity varies in diseased kidneys (MRD and CC) when compare to NR.

Formulation of pre-processing procedure: The pre-processing procedure prior to feature extraction must be formulated such that the sonographic information of kidney region is preserved. Hence care has been taken to ensure, no alteration in the spatial gray level distribution particularly in kidney region. The steps involved in proposed pre-processing procedure, as illustrated in the Fig. 2. that concern above requirement are image segmentation, image rotation and unbounded pixel elimination.

Segmentation is a fundamental process for higher level medical image analysis. In the present work, i-HSIC segmentation scheme have been used for contouring the kidney region of different kidney categories. This scheme is preferred as it provides a general solution for contouring. Also the comparative study with other three segmentation schemes namely, Modified Snake Model Contour (MSMC) (Kass *et al*., 1988; Cohen, 1991), Markov Random Field Contour (MRFC) (Marcos and Carlos, 2005; Chen and Metaxas, 2000) and Expert Outlined Contour (EOC) shows i-HSIC perform well to retain the Pixels-Of-Interest (POI) that reflects the characteristic of the kidney in all three categories. The contour obtained using i-HSIC segmentation scheme for NR image is shown in the Fig. 2.

Usually the transducer probe position is adjusted during scanning for better sonographic visualization (Hagen, 1995). This results in different orientation of kidney region as can be seen in the Fig. 3. In the acquired image, kidney may geometrically be viewed as elliptic. The visual inspection confirms that the major axis makes an angle θ (called as angle of inclination) with respect to the horizontal or reference axis and it varies anywhere between 0 to 180°. Before feature extraction, the images are to be rotated to ensure $\theta = 0°$. This is performed to

Fig.1 a: Normal image of male with age 38 years, b. Medical renal diseases image of male with age 45 years and c. Cortical polycystic disease image of female with age 51 years

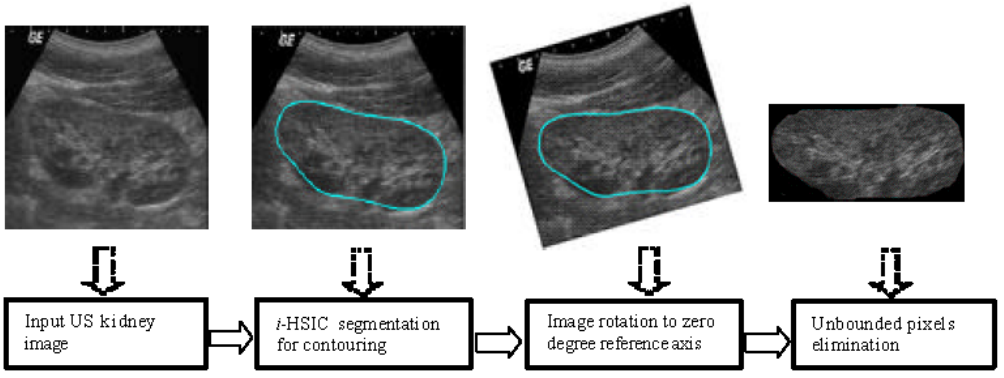

Fig. 2: Pre processing steps to retain POI in US kidney images

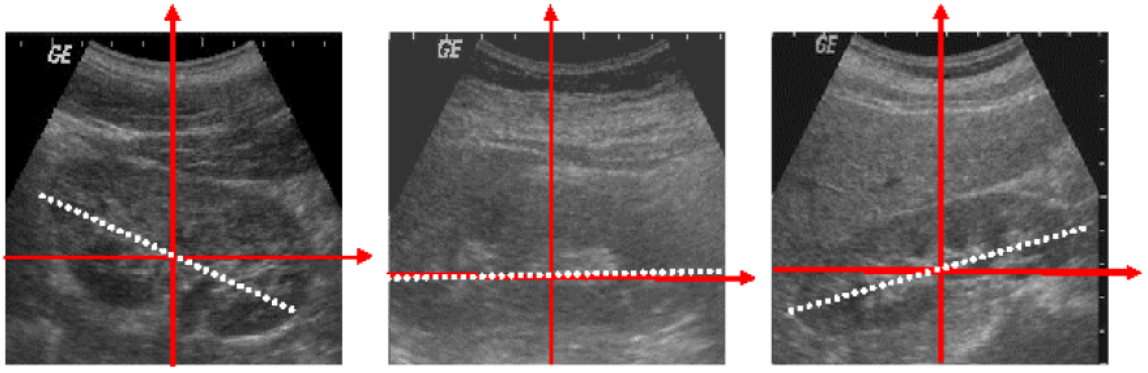

Fig. 3: US kidney Image of three different normal subjects showing the orientation of major axis at an angle 'θ' measured anticlockwise with respect to horizontal axis. For (a). θ = 157°, (b). θ = 2°, and (c). θ = 32°

maintain uniformity in image representation, avoid influence of varied orientation on features and define angular radial cut-off frequencies at identical regular interval for all images. The determination of major axis orientation and the estimation of angle of inclination θ are made by using the co-ordinates of i-HSIC contour.

In general, the contour can be defined as a series of points in polar co-ordinate (Friedland and Rosenfeld, 1989) and can be represented by a vector $C = \{c_1, c_2, c_3 \ldots, c_L\}$, where L is the number of points in the contour. Each c is an ordered pair of the x and y co-ordinates of a point on the contour. The co-ordinates of a particular point c_p in the contour is taken as a reference initially and distant measure d is estimated between c_p and all points c_q. This process is repeated until all the points in the contour have been considered as reference. This results in p maximum distance measures. The co-ordinates of the points that are dislocated farthest (c_i, c_j) is obtained by finding the maximum of p maximum distance measures as given in Eq. 1.

$$D_{max}(c_i, c_j) = \max\left[\max_p \{d(c_p - c_q)\}\right] \quad (1)$$

Where c_i and c_j are the co-ordinates of the points that are dislocated farthest

$$p,q = 1,2,3,\ldots..L$$

The slope of the major axis and hence the θ can be determined from c_i and c_j value. Based on calculated θ, the image is rotated so that the major axis of kidney region is oriented exactly on the horizontal axis (Fig. 2).

After the contour estimation and followed by rotation, it becomes necessary to eliminate the superfluous echoes that lie outside the kidney region. The pixels enclosed by the contour 'C' are considered to be POI or bounded pixel $p_B(x,y)$ and pixels lies outside the contour 'C' are regarded as unbounded or noise pixels $p_U(x,y)$. The histogram analysis of three kidney categories

shows that the gray level intensity values of these pixels vary within the range 4-228. Therefore, gray level intensity value of contour pixels are assigned as 255 to demarcate $p_B(x,y)$ from $p_U(x,y)$. In order to eliminate $p_U(x,y)$, the gray level value of $p_U(x,y)$ is compared with contour pixel value. If $p_U(x,y) = 255$, then $p_U(x,y) = 0$ outside 'C'. The $p_B(x,y)$ is retained with same intensity value as that of acquired image I(x,y) inside 'C'. This results in a pre-processed image $I_B(x,y)$ of size MxN, where 'M' is the image height and N is the image width, that contains only the Pixels-Of-Interest (POI) as depicted in the Fig. 2.

Power spectrum estimation and feature extraction: A 2-D Fast Fourier transform (2-D FFT) algorithm is applied to the preprocessed image $I_B(x,y)$ and magnitude square of the spectral components F(u,v) is computed to obtain power spectrum P(u,v) (Gonzales and Woods, 1999; Anil, 2000) by using the Eq. 2 and 3.

$$F(u,v) = \frac{1}{MN}\sum_{x=0}^{M-1}\sum_{y=0}^{N-1} I_B(x,y)\exp\left[-j2p\left(ux/M + vy/N\right)\right] \quad (2)$$

for u = 0, 1, 2,……, M-1 and v = 0, 1, 2,……, N-1.

$$P(u,v) = \left|F(u,v)\right|^2$$

In the power spectrum the angular radial cut-off frequencies (Ω_{rcn}) are defined at regular interval to evaluate a set of proposed power spectral features. As physical dimension of the pre-processed image is represented by MxN, the resultant P(u,v) will also have the same dimension. Suppose N>M, then Ω_{rcn} are to be defined along M direction and the maximum angular radial cut-off frequency $\Omega_{rc}(max)$ achieved is π, specified at regular intervals $\{0, 2\pi/M, 4\pi/M, 6\pi/M,\ldots, \pi\}$. The corresponding angular radial distances (Ω_{rdn}) are given at interval {0, 1, 2, 3,…, M/2}(Fig. 4). Similarly if M>N, then Ω_{rcn} are defined at intervals $\{0, 2\pi/N, 4\pi/N, 6\pi/N,\ldots, \pi\}$ with Ω_{rdn} at {0, 1, 2, 3,…, N/2}. Hence the definition of Ω_{rcn} and Ω_{rdn} varies with image size and direction. It can also be observed that any further extension of maximum angular radial distance $\Omega_{rd}(max)$ beyond M/2 or N/2 is not possible (Prabhu *et al*., 2001).

The solution for extending $\Omega_{rd}(max)$ is achieved by two means: Computing 2-D FFT for $I_B(x,y)$ after Symmetrical Zero Padding (SZP) and Extending $\Omega_{rd}(max)$ upto

$$d = \left[\left(\frac{M}{2}\right)^2 + \left(\frac{N}{2}\right)^2\right]^{1/2}$$

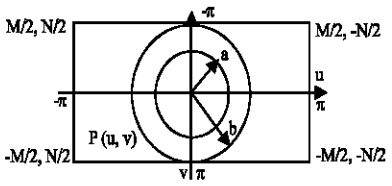

Fig. 4: The angular radial cut-off frequencies are defined at 'a' and 'b'. Here N>M. The Ω_{rd} of 'a' to specify Ω_{rc} is within $0 \le \Omega_{rda} \le$ b, where b ≤ Ω_{rd} (max) = M

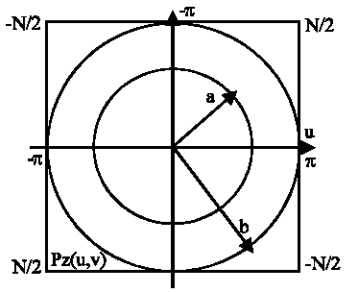

Fig. 5: The angular radial cut-off frequencies are defined at 'a' and 'b' after SZP. Here M = N. The Ω_{rd} of 'a' to specify Ω_{rc} is within $0 \le \Omega_{rda}$ = b, where b = Ω_{rd} (max) = M = N. But P(u,v) and Pz(u,v) are not equal

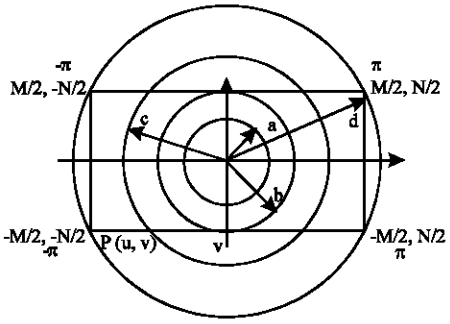

Fig. 6: The angular radial distance defined at 'a', 'b' 'c' and'd'. Here N>M. The Ω_{rd} of 'a' to specify Ω_{rc} is within $0 \le \Omega_{rda} \le$ b, where b = M and can be further extended upto $d = \Omega_{rd}(max)\left[\left(\frac{M}{2}\right)^2 + \left(\frac{N}{2}\right)^2\right]^{1/2}$

In first method, $\Omega_{rd}(max)$ is either M or N [∴M = N], but the P(u,v) before and after SZP are not identical. The only advantage of this method is Ω_{rcn} and Ω_{rdn} can be defined at same intervals irrespective of image size and direction as represented in the Fig. 5. The optimum solution may be achieved by the proposed second method. By referring the Fig. 6, it can be seen that Ω_{rdn} may be defined anywhere between 1 to d, which includes all the power

spectral components from low to high spatial frequencies. This facilitates to have flexibility in defining Ω_{rdn} and Ω_{rcn} irrespective of image size and direction. Also P(u,v) is preserved without any change. In this method, the Ω_{rcn} are defined at regular intervals $\{0, \pi/d, 2\pi/d, 3\pi/d,\ldots, \pi\}$ with Ω_{rdn} at $\{0, 1, 2, 3,\ldots, d\}$. Now the proposed power spectral features can be estimated.

A set of 'N' window functions $W_1(u,v)$, $W_2(u,v)$,….., $W_N(u,v)$ having specific lower and upper cut-off frequencies are applied over the power spectrum at the regular interval, as given in the Eq. 4.

$$W_n(u,v) = \begin{cases} 1 & O_{rcn}(l)\, O_{rc} \le O_{rcn}(u) \\ 0 & \text{elseehere} \end{cases} \quad (4)$$

Where

n = 1,2,3,….,N

N = d/L is the number of window functions

L is the length of the window measured in pixel radians

$\Omega_{rc}(l)$ is the lower angular radial cut-off frequency measured in pixel radian

$\Omega_{rc}(u)$ is the upper angular radial cut-off frequency measured in pixel radian

The selection of window length is arbitrary. For L = 1, the window functions N available are d. In the present research, it will be shown that for a constant length of L = 10, the derived features provide appreciable discrimination between 3 kidney categories. Therefore, the window functions available are d/10. The fixing of window emphasis to a ssign lower and upper cut-off frequency to each window as detailed in the Table 1. The power spectral components $P_n(u,v)$ that corresponds to each window is obtained by multiplying P(u,v) with $W_n(u,v)$. Using these power spectral components the power spectral features $P_T^{W_1}$, $P_T^{W_2}$, $P_{T-W_{12}}^{R_1}$, $P_{T-W_{12}}^{R_2}$, $P_{T-W_{1d}}^{R_3}$ and $P_{T-W_{1d}}^{R_4}$ are estimated by using the Eq. 5-10.

If the power spectral components within the window $W_1(u,v)$ is denoted by $P_1(u,v)$, then the total power under $W_1(u,v)$ is represented by $P_T^{W_1}$ as given in Eq. 5.

$$P_T^{W_1} = \sum_{u,v=O_{rc1(l)}}^{O_{rc1(u)}} \sum P_2(u,v) \quad (5)$$

The lower cut-off frequency $\Omega_{rc1}(l)$ of window is 1 (i.e., it does not include DC component) and the upper cut-off frequency $\Omega_{rc1}(u)$ is $10\pi/d$. Using the power spectral components $P_2(u,v)$ obtained with $W_2(u,v)$, the second feature $P_T^{W_2}$, defined as the total power within $W_2(u,v)$ is estimated as mentioned in the Eq. 6:

$$P_T^{W_2} = \sum_{u,v=O_{rc2(l)}}^{O_{rc2(u)}} \sum P_2(u,v) \quad (6)$$

Here the lower cut-off frequency $\Omega_{rc2}(l)$ and upper cut-off frequency $\Omega_{rc2}(u)$ is $11\pi/d$ and $20\pi/d$, respectively Table 1.

The influence of power spectral components of NR, MRD and CC image data set on the features $P_T^{W_1}$ and $P_T^{W_2}$ can be studied by two parameters, global mean total power within windows $W_1(u,v)$ and $W_2(u,v)$ and global mean total power within all the windows, $W_1(u,v)$ to $W_N(u,v)$. Using these parameters, four power ratio's are defined as represented in Eq. 7-10 to study the efficacy of $P_T^{W_1}$ and $P_T^{W_2}$ and to identify the kidney category.

$$P_{T-W_{12}}^{R_1} = \frac{P_T^{W_1}}{\frac{1}{K}\sum_{i=1}^{K}\left(P_T^{W_1}(i) + P_T^{W_2}(i)\right)} \quad (7)$$

Table 1:Power spectral components $P_n(u,v)$ and respective window functions $W_n(u,v)$ having specific lower and upper angular radial cut-off frequencies

Sl.No.	Window function $W_n(u,v)$	Length of window (L)	Lower and upper cut-off frequency $\Omega_{rcn}(l) \le \Omega_{rc} \le \Omega_{rcn}(u)$	Power spectral component $P_n(u,v)$
1	$W_1(u,v)$	10	$1 \le \Omega_{rc} \le 10\pi/d$	$P_1(u,v) = P(u,v) \times W_1(u,v)$
2	$W_2(u,v)$	10	$11\pi/d \le \Omega_{rc} \le 20\pi/d$	$P_2(u,v) = P(u,v) \times W_2(u,v)$
3	$W_3(u,v)$	10	$21\pi/d \le \Omega_{rc} \le 30\pi/d$	$P_3(u,v) = P(u,v) \times W_3(u,v)$
4	$W_4(u,v)$	10	$31\pi/d \le \Omega_{rc} \le 40\pi/d$	$P_4(u,v) = P(u,v) \times W_4(u,v)$
5	$W_5(u,v)$	10	$41\pi/d \le \Omega_{rc} \le 50\pi/d$	$P_5(u,v) = P(u,v) \times W_5(u,v)$
6	$W_6(u,v)$	10	$51\pi/d \le \Omega_{rc} \le 60\pi/d$	$P_6(u,v) = P(u,v) \times W_6(u,v)$
7	$W_7(u,v)$	10	$61\pi/d \le \Omega_{rc} \le 70\pi/d$	$P_7(u,v) = P(u,v) \times W_7(u,v)$
8	$W_8(u,v)$	10	$71\pi/d \le \Omega_{rc} \le 80\pi/d$	$P_8(u,v) = P(u,v) \times W_8(u,v)$
9	$W_9(u,v)$	10	$81\pi/d \le \Omega_{rc} \le 90\pi/d$	$P_9(u,v) = P(u,v) \times W_9(u,v)$
10	$W_{10}(u,v)$	10	$91\pi/d \le \Omega_{rc} \le 100\pi/d$	$P_{10}(u,v) = P(u,v) \times W_{10}(u,v)$
11	$W_{11}(u,v)$	10	$101\pi/d \le \Omega_{rc} \le 110\pi/d$	$P_{11}(u,v) = P(u,v) \times W_{11}(u,v)$
12	$W_{12}(u,v)$	10	$111\pi/d \le \Omega_{rc} \le 120\pi/d$	$P_{12}(u,v) = P(u,v) \times W_{12}(u,v)$
13	$W_{13}(u,v)$	10	$121\pi/d \le \Omega_{rc} \le 130\pi/d$	$P_{13}(u,v) = P(u,v) \times W_{13}(u,v)$
14	$W_{14}(u,v)$	10	$131\pi/d \le \Omega_{rc} \le \pi$	$P_{14}(u,v) = P(u,v) \times W_{14}(u,v)$

$$P_{T-W_{12}}^{R_2} = \frac{P_T^{W_2}}{\frac{1}{K}\sum_{i=1}^{K}\left(P_T^{W_1}(i) + P_T^{W_2}(i)\right)} \quad (8)$$

$$P_{T-W_{1N}}^{R_3} = \frac{P_T^{W_1}}{\frac{1}{K}\sum_{i=1}^{K}\left(P_T^{W_1}(i) + P_T^{W_2}(i) + \ldots\ldots + P_T^{W_N}(i)\right)} \quad (9)$$

$$P_{T-W_{1N}}^{R_4} = \frac{P_T^{W_2}}{\frac{1}{K}\sum_{i=1}^{K}\left(P_T^{W_1}(i) + P_T^{W_2}(i) + \ldots\ldots + P_T^{W_N}(i)\right)} \quad (10)$$

Where K is the total number of images in the database.

$P_T^{W_1}(i)$, $P_T^{W_2}(i)$ and $P_T^{W_N}(i)$ are the global total power of respective windows estimated by considering all the images in the database.

Such global parameters are used to measures the stability of features $P_T^{W_1}$ and $P_T^{W_2}$ in discrimination, if any exclusion or inclusion of images in the database is made. Any change in data set may alter global parameters value to the extent that classification may fail. Therefore, in-depth analysis on these power ratio's is necessary to identify their non-overlapping range by finding the minimum and maximum tolerable value of denominator terms in the Eq. 7-10 to ensure acceptable classification of kidney categories.

RESULTS

The power spectrum P(u,v) of the pre-processed images for NR, MRD and CC is shown in the Fig. 7. The low frequency components are centered and high frequency components are distributed angularly through shifting and folding operations. The visual inspection of the spectrum confirms the absence of any conclusive distribution of spectral components that provides basic knowledge on kidney category. This emphasizes the need for establishing reliable power spectral features to investigate the power spectrum. For this purpose, specific cut-off frequencies are defined in the spectrum as given in the Fig. 8. Since the pre-processed images have dimension of 120× 252, the value for 'd' is 140. With L = 10, the Ω_{rcn} can be defined at intervals {0, 10π/14, 20π/14, 30π/140,…, π} with corresponding Ω_{rdn} at {0, 10, 20, 30,…, 140}. Therefore the total number of window functions available for power spectrum study is 14. The $P_n(u,v)$ within each window $W_n(u,v)$ having specific lower $\Omega_{rcn}(l)$ and upper $\Omega_{rcn}(u)$ cut-off frequencies Table 1 are then evaluated and investigated.

The Fig. 9 shows the variation of Cumulative Total Power (CTP) for the images of respective kidney category, measured at upper cut-off frequencies $\Omega_{rcn}(u)$, from 10π/140 to π. It can be seen that the CTP for MRD is high followed by NR and CC. But for few images the total power $P_T^{W_n}$ within each window gets overlaps with inter category and impedes the process of classification. The variation of total power within each window is shown in the Fig. 10. It is evident that the total power $P_T^{W_1}$ and $P_T^{W_2}$ calculated by using the windows $W_1(u,v)$ and $W_2(u,v)$ are well separated. For other windows functions, $W_3(u,v)$ to $W_{14}(u,v)$, the total power gets indistinguishable. As the total power of windows $W_1(u,v)$ and $W_2(u,v)$ offers better separation in their values for inter category, the maximum and minimum values of $P_T^{W_1}$ and $P_T^{W_2}$ are estimated by considering all the images. The result obtained is shown

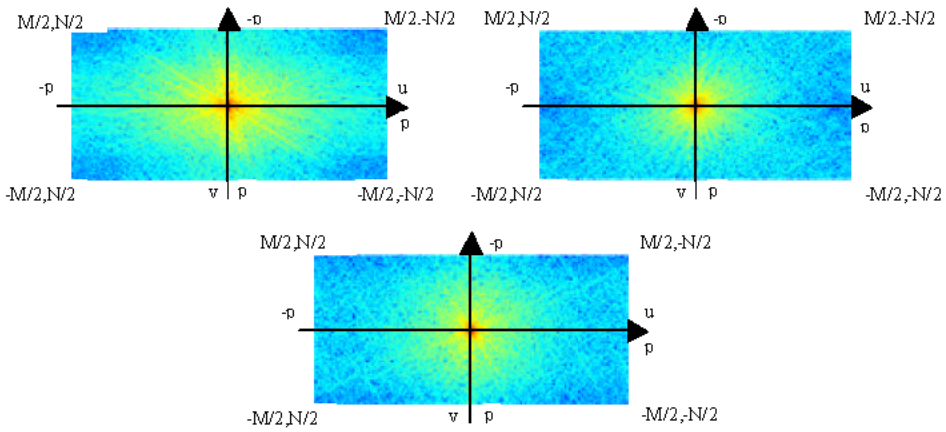

Fig. 7: The power spectrum P(u,v) of NR, MRD and CC US images of (a). Male subject of age 51.9 (b). Female subject of age 56.2 (c). Male subject of age 49.5. The low frequency power spectral components are centered and distributed angularly

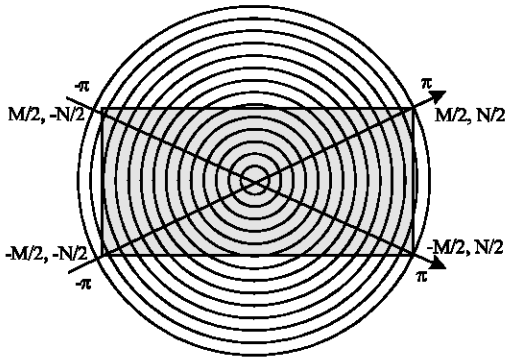

Fig. 8: The angular radial cut-off frequencies defined diagonally upto $d = \Omega_{rd}\ (max)\left[\left(\frac{M}{2}\right)^2+\left(\frac{N}{2}\right)^2\right]^{1/2} =$ at regular interval of 10 pixel radians. The number of available windows is 14

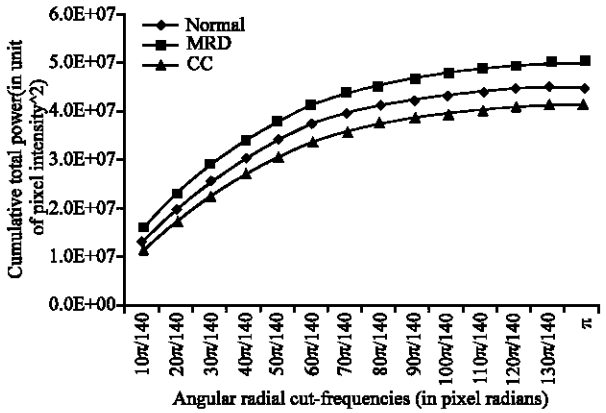

Fig. 9: Variation in Cumulative Total Power (CTP) measured at $\Omega_{rcn}(u) = 10\pi/140$ to π

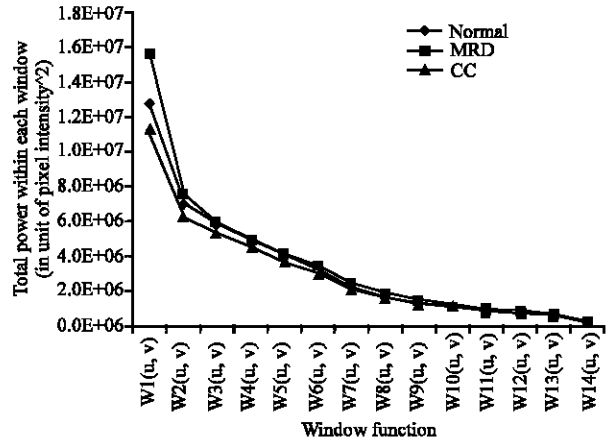

Fig. 10: Variation in total power $\left(P_T^{W_n}\right)$ within each window functions having specific lower and upper cut-off frequencies

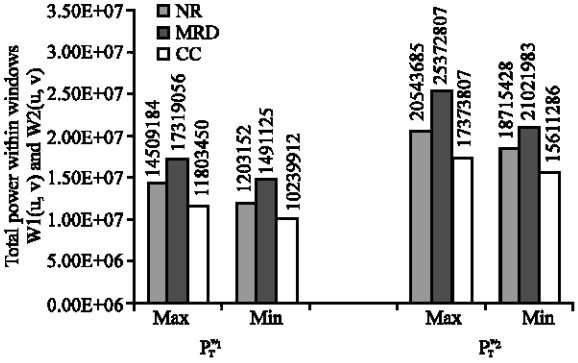

Fig. 11: The maximum and minimum value of mean total power $P_T^{W_1}$ and $P_T^{W_2}$

in the Fig. 11. The attempt has been made to study the effect of global mean power parameters on $P_T^{W_1}$ and $P_T^{W_2}$ in classifying the kidney category using power ratio's. For this purpose the maximum allowable limit of denominator of Eq. 7 and 8 which gives the mean total power of first and second window and the denominator of Eq. 9 and 10 that provides mean total power of all the 14 windows is evaluated and presented.

DISCUSSION

It can be seen from the Fig. 9, the CTP increases from 12816668 to 45128164 for NR, 15695925.8 to 50309728.8 in case of MRD and it varies between 11283633.2 and 41677921.3 for CC. Generally the tissue characteristics of kidney determine the magnitude of CTP. In MRD, sonographic evaluation demonstrates unclear differentiation between renal sinus, medulla and cortex region, due to tissue destruction. As kidney region appears to be hyper echoic with high and widely varying spatial gray level intensity values, larger value of CTP over the angular radial frequency may be observed. For NR, the hyper echoic components are less compared to MRD, because of hypo echoic medulla and surrounding cortex. This leads to lesser CMTP for NR compared to MRD. In case of CC, the sonographic evaluation of renal cyst is a circular hypo echoic mass with good through transmission. For poly cystic diseases, the cyst may be large enough to obliterate the renal sinus and multiple circular hypo echoic masses at isolated location in renal parenchyma may be seen. This results in more hypo echoic cystic region with low variation in spatial gray level intensity. Therefore, the CTP for CC is less against NR and MRD. Though the anatomical definitions are clearly reflected in the quantitative measure CTP, there exist overlapping between inter category.

The distribution of total power contained within the each window is depicted in the Fig. 10. As the total power of window functions $W_3(u,v)$ to $W_{14}(u,v)$ gets overlap for three kidney category, it becomes impossible to differentiate the category using these power spectral components. Hence these components are not helpful for classification and not been considered for the analysis. But the total power within the window functions $W_1(u,v)$ and $W_2(u,v)$ are well separated and more insight has been given for further investigation on $P_T^{W_1}$ and $P_T^{W_2}$. The minimum and maximum value of $P_T^{W_1}$ for NR is 12013152 and 14509184, in case of MRD the obtained value is 14971125 and 17319056 and for CC the value is 10239912 and 11803450. The evaluation of $P_T^{W_2}$ indicates that the maximum and minimum value for NR, MRD and CC is 20543685 and 18715428, 25372807 and 21021983, 17373807 and 15611286, respectively. The study on $P_T^{W_1}$ and $P_T^{W_2}$ reveals the existence of definite and discrete range of values for all three kidney categories. This proves the performance of the features $P_T^{W_1}$ and $P_T^{W_2}$ in identification and classification of kidney.

The global parameters, the mean total power of first and second window Eq. 7 and 8 and mean total power of all the windows Eq. 9 and 10 are calculated by taking into account all the images in database. The values obtained for these terms are 20041895 and 45705271. In order to identify their maximum tolerable limit in case any modification in data base is made further analysis on mean total power terms is carried out. The results indicate that the non-overlapping range of mean total power for the feature $P_T^{W_1}$ is 19692043 = 20041895 = 20397990 and for $P_T^{W_2}$ is 19585896 = 20041895 = 20508511. Likewise the non-overlapping range of mean total power of all the windows in case of $P_T^{W_1}$ is 44907529 = 45705271 = 46517349 and for $P_T^{W_2}$ is 44665428 = 45705271 = 46769386. Therefore, if the variations of these global mean total power parameters are within the derived limit, the features $P_T^{W_1}$ and $P_T^{W_2}$ maintain their stability and provide reliable classification of kidney category. Also it can be seen, compared to $P_T^{W_1}$ better range is offered by $P_T^{W_2}$. This shows that the power spectral components of window $W_2(u,v)$ allow increased change in the mean total power. Using these global mean total powers, the power ratio features are evaluated and results are depicted in Table 2. It can be noticed that for each kidney category, the discrete range persists which ensure efficient identification. This indicates that any change in global parameters is within the specified limit the power ratio features may also be used for objectively classification of kidney.

The analysis of the US kidney images by the proposed features proves the efficacy of power spectral c omponents in fulfilling the requirements of CAD system.

Table 2: Power ratio's evaluated for three kidney categories using global mean total power parameters

	Kidney category		
Power ratio's	NR	MRD	CC
$P^{R_1}_{T-W_{12}}$	0.5994-0.7239	0.7470-0.8641	0.5109-0.5889
$P^{R_2}_{T-W_{12}}$	0.9338-1.0250	1.0489-1.2660	0.7789-0.9338
$P^{R_3}_{T-W_{14}}$	0.2628-0.3175	0.3276-0.3789	0.2240-0.2583
$P^{R_4}_{T-W_{14}}$	0.4094-0.4495	0.4599-0.5551	0.3415-0.3801

The category of kidney has been identified and in turn quantified with the values of the features. These numerical values provide a universal reference for each category. This facilitates to perform objective diagnosis by comparing similar past cases. The availability of numerical result also explores the possibility of implementing CAD system exclusively for US kidney images.

CONCLUSION

In this study, a new method for diagnosing and classifying the US kidney images is proposed. The power spectral features are obtained by defining angular radial cut-off frequencies at specified interval in the spectrum. It has been identified the power spectral components within the cut-off frequencies $1 \leq \Omega_{rc} \leq 10\pi/d$ and $11\pi/d \leq \Omega_{rc} \leq 20\pi/d$ are highly significant in categorization of images as NR, MRD and CC. The definite and discrete range of feature values exists between the categories. For the purpose of stability measure the variation of these features with respect to global mean total power is investigated. The maximum allowable limit beyond which the stability fails is identified and presented. The study reveals that the method not only helps in classification but also extends its potential in diagnosing and developing the CAD system for US kidney images. Further investigation on values of the parameters can be made for early detection of pathology that finds extensive application in clinical diagnosis.

REFERENCES

Abouzar Eslami, Shohreh Kasaei and Mehran Jahed, 2004. Radial Multi-scale Cyst Segmentation in Ultrasound Images of Kidney. IEEE. Proc. 4th Int. Symposium on Signal Processing and Information Technology, Rome, Italy, 1: 42-45.

Allemann, N., R.H. Silverman, D.Z. Reinstein and D.J. Coleman, 1993. High-frequency ultrasound imaging and spectral analysis in traumatic hyphema. Opthalmology, 100: 1351-1357.

Anil, K. Jain, 2000. Fundamentals of Digital Image Processing, Prentice-Hall.

Bakker, J., M. Olree, R. Kaatee, E.E. de Lange and R.J.A. Beek, 1997. In vitro Measurement of Kidney Size: Comparison of Ultrasonography and MRI", Ultrasound Med. Biol., 24: 683-688

Barbara Brunet-Imbault, Gerald Lemineur, Christine Chappard, Rachid Harba and Claude-Laurent Benhamou, 2005. A new anisotropy index on trabecular bone radiographic images using the fast Fourier transform. BMC. Medical Imaging, 5: 4.

Bommanna, R.K., M. Madheswaran, K. Thyagarajah, M.R.S. Reddy and S. Swarnamani, 2003. Efficient Information System for Health Care-Study and Implementation Methodology, IETE. Technical Rev., 20: 387-394.

Cohen, L.D., 1991. On Active Contour Models and Balloons. CVGIP - Image Understanding, 53: 211-218.

Eslami, A., M. Jahed and M. Naroienejad, 2005. Fully Automated Cyst Segmentation in Ultrasound Images of Kidney. Proceeding of 3rd IASTED International Conferencce Biomedical Engineering, Austria, Paper ID-19418.

Feleppa, E.J., J. Machi, T. Noritomi, T. Tateishi, R. Oishi, E. Yanagihara and J. Jucha, 1997. Differentiation of metastatic from benign lymph nodes by spectrum analysis in vitro. IEEE. Proc. Ultrasonics Symposium, 2: 1137-1142.

Friedland, N.S. and A. Rosenfeld, 1989. Ventricular Cavity Boundary Detection from Sequential Ultrasound Images using simulated Annealing. IEEE. Trans. Med. Imag., 8: 344-353.

Fukushima, M., K. Ogawa, T. Kubota and N. Hisa, 1997. Quantitative Tissue Characterization of Diffuse Liver Diseases from Ultrasound Images by Neural Network. IEEE. Proc. Nuclear Symposium, 2: 1233-1236.

Golub, R.M., R.E. Parsons, B. Sigel, E.J. Feleppa, J. Justin, H.A. Zaren, M. Rorke, J. Sokil-Melgar and H. Kimitsuki, 1993. Differentiation of breast tumors by ultrasonic tissue characterization, J. Ultrasound Med., 12: 601-608.

Gonzales, R. and R. Woods, 1999. Digital Image Processing, Addison-Wesley.

Gregory, J.S., R.M. Junold, P.E. Undrill and R.M. Aspden, 1999. Analysis of trabecular bone structure using Fourier transforms and neural networks. IEEE . Trans. Inform. Tech. Biomed., 3: 289-294.

Hagen-Ansert, S., 1995. Urinary System In: Diagnostic Ultrasound, (4th Edn.), St. Louis, MO: Mosby/ Elsevier.

Jun Xie, Yifeng Jiang and Hung-tat Tsui, 2005. Segmentation of kidney from ultrasound images based on texture and shape priors. IEEE. Trans. Med. Imag., 24: 45-57.

Karthikeyini, C., R.K. Bommanna and M. Madheswaran, 2004. Study on Ultrasound Kidney Images using Principal Component Analysis: A Preliminary Result", Proceeding of 4th Indian Conference on Computer Vision, Graphics and Image Processing, ISI Kolkata, India, 1: 190-195.

Kass, M., A. Witkin and D. Terzopoulos, 1991. Snakes: Active Contour Models. Int. J. Comp. Vis., 1: 321-331.

Li, D., P.M. Meany, M.W. Fanning., Q. Fang, S.A. Pendergrass and T. Raynold, 2002. Spectrum analysis of microwave breast examination data and reconstructed images. IEEE. Proc. Int. Symposium Biomed. Imaging, 1: 62-65.

Loizou, C.P., C. Christodoulou, C.S. Pattischis, R.S.H. Istepanian, M. Pantziaris and A. Nicolaides, 2002. Speckle Reduction in Ultrasound Images of Atherosclerotic Carotid Plaque. IEEE Proc. 14th Int. Conf. Digital Signal Processing, Santorini, Greece, 1: 525-528.

Loizou, C.P., C.S. Pattichis, C.I. Christodoulou, R.S.H. Istepanian, M. Pantziaris and A. Nicolaides, 2005. Comparative Evaluation of Despeckle Filtering in Ultrasound Imaging of the Carotid Artery. IEEE. Trans. Ultra. Ferro. Freq. Control, 52: 1653-1669.

Marcos Martin-Fernandez and Carlos Alberola-Lopez, An, 2005. Approach for contour detection of human kidney from ultrasound images using markov random fields and active contours. Med. Image Anal., 9 : 1-23.

Matre, K., E.M. Stokke, D. Martens and O.H. Gilja, 1999. In vitro Volume Estimation of Kidneys using 3-D Ultrasonography and a Position Sensor. Eur. J. Ultrasound, 10: 65-73.

Pollack, H.M. and B.L. McClennan, 2000. Clinical Urography, (2nd Edn.), Philadelphia: W.B. Saunders/ Elsevier.

Prabhu, K.G., K.M. Patil and S. Srinivasan, Diabetic feet at risk: A new method of analysis of walking foot pressure images at different levels of neuropathy for early detection of plantar ulcers. Med. Biol. Eng. Comp., 39: 288-293.

Sheng-Fang Huang, Ruey-Feng Chang, Dar-Ren Chen and Woo Kyung Moon, 2004. Characterization of Speculation on Ultrasound Lesions. IEEE. Trans. Med. Imag., 23: 111-121.

Spencer, T., M.P. Ramo, D.M. Salter T. Anderson, P.P. Kearney, G.R. Sutherland, K.A. Fox and W.N. McDicken, 1997. Characterization of atherosclerotic plaque by spectral analysis of intravascular ultrasound: An in vitro methodology. Ultrasound Med. Biol., 23: 191-203.

Tokudome, T., K. Mizushige K. Ohmori, K. Watanabe, Y. Takagi, Y. Takano and H. Matsuo, 1999. Neurogenic regulation of basal tone coronary artery with mild artherosclerosis in humans: Observation using two-dimensional intravascular ultrasound. Angiology, 50: 989-996.

Veenland, J.F., J.L. Grashuis, E.S. Gelsema, 1998. Texture analysis in radiographs: The influence of modulation transfer function and noise on the discriminative ability of texture features, Med. Phys., 25: 922-936.

Yi, W.J., K.S. Park, Y.G. Min and M.W. Sung, 1997. Distribution mapping of ciliary beat frequencies of respiratory epithelium cells using image processing. Med. Biol. Eng. Comp., 35: 595-599.